ARTICLE

# Optimized co-solute paramagnetic relaxation enhancement for the rapid NMR analysis of a highly fibrillogenic peptide

Nur Alia Oktaviani[1] · Michael W. Risør[2] · Young-Ho Lee[3] · Rik P. Megens[4] ·
Djurre H. de Jong[1] · Renee Otten[1] · Ruud M. Scheek[1] · Jan J. Enghild[5] ·
Niels Chr. Nielsen[2] · Takahisa Ikegami[3,6] · Frans A. A. Mulder[1,2]

**Abstract** Co-solute paramagnetic relaxation enhancement (PRE) is an attractive way to speed up data acquisition in NMR spectroscopy by shortening the $T_1$ relaxation time of the nucleus of interest and thus the necessary recycle delay. Here, we present the rationale to utilize high-spin iron(III) as the optimal transition metal for this purpose and characterize the properties of its neutral chelate form Fe(DO3A) as a suitable PRE agent. Fe(DO3A) effectively reduces the $T_1$ values across the entire sequence of the intrinsically disordered protein α-synuclein with negligible impact on line width. The agent is better suited than currently used alternatives, shows no specific interaction with the polypeptide chain and, due to its high relaxivity, is effective at low concentrations and in 'protonless' NMR experiments. By using Fe(DO3A) we were able to complete the backbone resonance assignment of a highly fibrillogenic peptide from α₁-antitrypsin by acquiring the necessary suite of multidimensional NMR datasets in 3 h.

**Keywords** Paramagnetic relaxation enhancement · Intrinsically disordered proteins · Fe(DO3A) · α₁-Antitrypsin · Amyloid beta-peptides · NMR spectroscopy

Nur Alia Oktaviani and Michael W. Risør have equally contributed to this work.

✉ Frans A. A. Mulder
fmulder@chem.au.dk;
http://nmr.au.dk

[1] Groningen Biomolecular Sciences and Biotechnology Institute, University of Groningen, Groningen, The Netherlands

[2] Interdisciplinary Nanoscience Center (iNANO) and Department of Chemistry, University of Aarhus, Gustav Wieds Vej 14, 8000 Aarhus C, Denmark

[3] Institute for Protein Research, Osaka University, Suita, Japan

[4] Stratingh Institute for Chemistry, University of Groningen, Groningen, The Netherlands

[5] Interdisciplinary Nanoscience Center (iNANO) and Department of Molecular Biology and Genetics, University of Aarhus, Aarhus C, Denmark

[6] Present Address: Graduate School of Medical Life Science, Yokohama City University, 1-7-29 Suehiro-cho, Tsurumi-ku, Yokohama 230-0045, Japan

## Introduction

NMR spectroscopy has proven to be the most suitable methodology to obtain insight into the details of protein conformational disorder that exists in all branches of life as multifunctional and flexible interaction domains, proteins or peptides (Uversky and Longhi 2010). The study of these intrinsically disordered regions (IDRs) or proteins (IDPs) imposes technical challenges arising from the low dispersion of NMR chemical shifts. The very small differences in the magnetic environment of the nuclei cause spectral congestion and resonance overlap, demanding time-consuming higher dimensional experiments or specific pulse sequence designs to resolve signal ambiguities (Bermel et al. 2006b; Sakhaii et al. 2013; Takeuchi et al. 2010). The hyperdimensional NMR experiments involve many magnetization transfer steps, and are compromised in sensitivity by spin–spin relaxation during successive periods of coherent evolution. In addition, several unfolded polypeptides are inherently unstable or aggregation-prone under the concentrations necessary for multidimensional NMR experiments, setting constraints on the available experimental time. This includes several amyloid peptides, notoriously known to self-associate and aggregate, where a

growing interest in the early amyloid conversion processes and soluble intermediate structures (Schmit et al. 2011) have created the need for contemporary experimental strategies that enable NMR spectroscopic studies within the sample half-life.

To face these challenges, several approaches have been proposed in the literature that increase the signal per unit time (Kupce and Freeman 2004; Marion 2005; Schanda et al. 2006), whereof speeding up nuclear spin relaxation represents an attractive solution. The longitudinal relaxation time ($T_1$) describes the return time of magnetization along the polarizing field axis. For flexible molecules, this time constant can be on the order of 1 s, which makes recycle delays consume most of the NMR recording time. Ideally, this idle time should be reduced to zero, which would allow improved sensitivity and resolution through faster data acquisition. In a number of applications to proteins, amide proton relaxation rates were increased through the application of selective $^1$H pulses (Diercks et al. 2005; Pervushin et al. 2002; Schanda et al. 2006). An alternative, and fully tunable strategy would be the use of paramagnetic co-solutes, as the protein relaxation rates increase proportionally to the concentration of paramagnetic agent (Cai et al. 2006; Caravan 2009).

Small polar, neutral paramagnetic chelates are expected to be best suited, since these minimize the chance of persistent interactions due to hydrophobic and electrostatic interactions between the PRE co-solute and amino acid side chains, while at the same time providing excellent solubility in watery milieus. In addition, the proximity of the paramagnetic agent to all protein nuclei in unfolded polypeptide chains and IDPs makes co-solute PRE highly suitable for speeding up $T_1$ relaxation in these cases. In contrast, PRE effects in folded proteins are limited to surface residues. In these cases, fast data acquisition by reduction of the interscan delay would lead to strong attenuation of signals from the protein core. Previous studies have shown that neutral nickel(II)-chelate PRE-agents [such as Ni(DO2A)] enhance longitudinal relaxation rates with negligible effects on proton line widths (Cai et al. 2006; Theillet et al. 2011). However, due to very short $T_{1e}$ and $T_{2e}$ times of Ni(II), relatively high concentrations (>30 mM) are necessary to reduce protein $^1$H $T_1$ values significantly, and, in addition, since the PRE scales with the square of the magnetogyric ratio, nickel is not suited to reduce $^{13}$C relaxation times in proton-less applications, which have been demonstrated to be beneficial for NMR spectroscopy of IDPs close to physiological conditions (Bermel et al. 2006a; Hsu et al. 2009). At the other extreme, efficient relaxation agents with long electron relaxation times, such as Gd$^{3+}$, are not suited either, as these produce a preferential increase in $R_{2p}$, and therewith lead to strong line broadening (Bertini et al. 2001).

In this work, we put forward a suitably optimized PRE chelate agent, Fe(DO3A), for the study of peptides and proteins by liquid-state NMR spectroscopy. The use of high-spin iron(III) as the optimal transition metal for $T_1$ relaxation enhancement is theoretically rationalized through its specific electron spin relaxation time and the associated contribution to the dipolar relaxation enhancement. We successfully applied the agent to obtain the complete liquid-state resonance assignment of a highly fibrillogenic peptide derived from the C-terminal tail of the serine protease inhibitor α$_1$-antitrypsin, where previous attempts to determine the solution structure of this peptide by NMR spectroscopy proved unsuccessful due to sample instability. The use of Fe(DO3A) presents a rapid and versatile strategy for the study of this type of short-lived soluble samples. As many other biologically and medically relevant peptides and proteins self-associate, reduction of the experimental time below sample half-life is of fundamental importance.

## Theory

### Theoretical rationale for the optimal PRE agent to obtain nuclear $T_1$ shortening

The co-solute paramagnetic relaxation enhancement is critically dependent on the relationship between the electron spin relaxation rates ($R_{1p}$ and $R_{2p}$) and the molecular bond vector reorientation time, $\tau_R$, of the protein of interest. The paramagnetic contribution to relaxation can be expressed as (Cai et al. 2006):

$$R_1 = R_{1d} + c \times R_{1p} \tag{1}$$

$$R_2 = R_{2d} + c \times R_{2p} \tag{2}$$

where $R_{1d}$ and $R_{2d}$ are the longitudinal and transverse relaxation rate in the absence of paramagnetic agent, respectively, $R_{1p}$ and $R_{2p}$ are relaxation contributions due to the electron–nuclear dipolar interaction, and $c$ is the concentration coefficient of the paramagnetic agent. An alternative notation is also widespread where the second terms in Eqs. (1) and (2) are replaced with the product of the concentration (in mM) of the paramagnetic agent, multiplied with the 'relaxivities' $r_1$ and $r_2$, defined as the experimental relaxation induced by 1 mM of the paramagnetic compound (Caravan 2009).

The paramagnetic relaxation enhancement through modulation of the electron–nuclear dipolar coupling, can be described as dominated by either rotational motion (inner-sphere relaxation, see Peters et al. 1996), or by the relative diffusion of the protein atoms and the paramagnetic compound (outer-sphere relaxation, see Abragam

1961; Freed 1978). Relaxation equations are available for both scenarios, with the important difference for the case of outer-sphere relaxation that (1) the concentration of the paramagnetic molecules enters the relaxation equations directly, rather than by a concentration coefficient [the latter expressing the fraction of molecules experiencing paramagnetic relaxation enhancement (PRE)] and (2) the spectral density functions include the relative translation diffusional motion of the two species. Pintacuda and Otting (2002) demonstrated that the inner-sphere approximation appears to be more appropriate for the interaction of gadodiamide with a globular protein. Cai et al. (2006) have equally applied this assumption in their description of Ni(DO2A) with the protein SUMO, and it will also be assumed in the analysis that follows. However, for the ensuing discussion, the exact mechanism of modulation of the electron–nuclear coupling is not important, as the relaxation rates show a similar dependence on the electron spin relaxation times due to either mechanism, albeit that the finer details of their frequency dependence are different (Bertini et al. 2001).

Following Peters et al. (1996) the 'inner-sphere' electron–nuclear dipolar contribution to the relaxation rate under influence of a single paramagnetic center is given by:

$$R_{1p} = \frac{2S(S+1)\gamma_I^2 g^2 \beta^2}{15r^6} \left(\frac{\mu_0}{4\pi}\right)^2 \left[\frac{3\,\tau_{c1}}{1+\omega_I^2\tau_{c1}^2} + \frac{7\,\tau_{c2}}{1+\omega_S^2\tau_{c2}^2}\right] \tag{3}$$

$$R_{2p} = \frac{S(S+1)\gamma_I^2 g^2 \beta^2}{15r^6} \left(\frac{\mu_0}{4\pi}\right)^2 \left[4\tau_{c1} + \frac{3\,\tau_{c1}}{1+\omega_I^2\tau_{c1}^2} + \frac{13\,\tau_{c2}}{1+\omega_S^2\tau_{c2}^2}\right] \tag{4}$$

Here, S is the electron spin quantum number of the paramagnetic ion, $\gamma_I$ is the magnetogyric ratio of nucleus I, g is the electron g factor, $\beta$ is the Bohr magneton, $\omega_I$ and $\omega_S$ are the Larmor frequencies of the nucleus I and electron S, respectively, and r is the distance between the electron and nuclear spin. The effective longitudinal ($\tau_{c1}$) and transverse ($\tau_{c2}$) nuclear correlation times are determined by the rotational correlation time ($\tau_R$) of the nucleus–electron vector and the electron relaxation times ($T_{1e}$ and $T_{2e}$ respectively) of the paramagnetic species, as follows:

$$\frac{1}{\tau_{c1}} = \frac{1}{\tau_r} + \frac{1}{T_{1e}} \tag{5}$$

$$\frac{1}{\tau_{c2}} = \frac{1}{\tau_r} + \frac{1}{T_{2e}} \tag{6}$$

The dominating term in the electron–nuclear relaxation contribution will thus depend on the effective electron relaxation time and varies by several orders of magnitude for transition metals (Table 1). This gives rise to markedly different paramagnetic $R_{1p}$ and $R_{2p}$ effects as a function of

**Table 1** Electron relaxation times for several metal ions (Bertini et al. 2001)

| Metal ions | Electron relaxation times ($T_{1e}$/ps) |
|---|---|
| Low-spin $Fe^{3+}$ | $\sim 1$ |
| $Ni^{2+}$ | $\sim 10$ |
| High-spin $Fe^{3+}$ | $\sim 100$ |
| $Gd^{3+}$, $Mn^{2+}$, $Cu^{2+}$ | $\sim 1000$–$3000$ |

$T_{1e}$, which is simulated in Fig. 1, assuming a correlation time of bond vectors of 2 ns. In terms of optimal properties for $T_1$ relaxation enhancement, the PRE agent should display high relaxivity (i.e., strong concentration effect) without causing a large contribution to $R_2$ (line broadening).

## Paramagnetic relaxation contribution as a function of $T_{1e}$

If the electron relaxation times $T_{1e}$, $T_{2e} < \tau_R$, they will dominate the effective correlation times (i.e., $\tau_{c1} \approx T_{1e}$ and $\tau_{c2} \approx T_{2e}$). When $T_{1e} \approx T_{2e}$ and $\omega_I\tau_c \ll 1$ and $\omega_S\tau_c \ll 1$, the longitudinal and transverse paramagnetic relaxation enhancements, given by Eqs. (3) and (4) then become equal:

$$R_{1p} \approx R_{2p} = \frac{20S(S+1)\gamma_I^2 g^2 \beta^2}{15r^6} \left(\frac{\mu_0}{4\pi}\right)^2 T_{1e} \tag{7}$$

In this case, $R_{1p}$ becomes proportional to the electron relaxation time $T_{1e}$. Therefore, a very short $T_{1e}$, leads to a very low $R_{1p}$ (Fig. 1a, left) necessitating a high concentration of paramagnetic agent for significant PRE effect. This is the case for $Ni^{2+}$ and low-spin $Fe^{3+}$ applied to small proteins or IDPs, where $T_{1e} \approx$ picoseconds, whereas $\tau_R \approx$ nanoseconds.

For high-spin $Fe^{3+}$, the electron relaxation time is longer than that of $Ni^{2+}$ (see Table 1), but still shorter than $\tau_R$. This condition, with a $T_{1e}$ around 100 ps, can be approximated by the following simplification of (3) and (4) as $\omega_I\tau_c < 1$ and $\omega_S\tau_c > 1$:

$$R_{1p} = \frac{6S(S+1)\gamma_I^2 g^2 \beta^2}{15r^6} \left(\frac{\mu_0}{4\pi}\right)^2 T_{1e} \tag{8}$$

$$R_{2p} = \frac{7S(S+1)\gamma_I^2 g^2 \beta^2}{15r^6} \left(\frac{\mu_0}{4\pi}\right)^2 T_{1e} \tag{9}$$

In this regime, proportionality between $R_{1p}$ and $R_{2p}$ is still maintained. Higher relaxivity is achieved with the longer electron relaxation time at the cost of only a marginal increase in $R_2$ compared to $R_1$. In addition, a higher spin quantum number will also lead to faster relaxation.
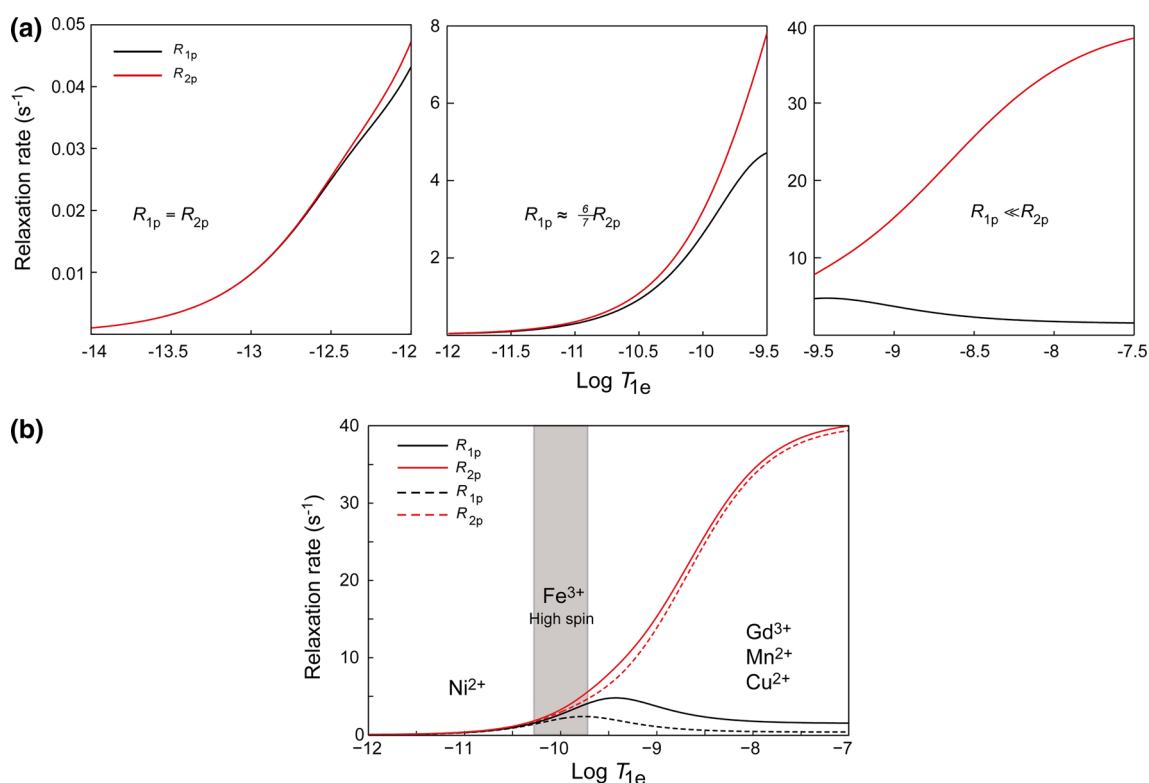
**Fig. 1** **a** Comparison of paramagnetic relaxation enhancements $c \times R_{1p}$ (=$c/T_{1p}$) and $c \times R_{2p}$ (=$c/T_{2p}$), due to co-solutes with different electron spin relaxation times, calculated using Eqs. (3) and (4). In these calculations the prefactor (square of the interaction strength) multiplied with the concentration coefficient equals $10^{10}$, the field strength used is 11.7 T (500 MHz) and the bond vector correlation time ($\tau_r$) is set to 2.0 ns. **b** Overview of the paramagnetic relaxation enhancements at field strengths of 500 MHz (*solid line*) or 1000 MHz (*dashed line*) with indication of the paramagnetic metal ions at their respective electron relaxation times. All simulation parameters, except $B_0$, are as in (**a**)

For high-spin $Fe^{3+}$, optimal PRE is thus ensured by a large relaxivity coupled with minimal line broadening (Fig. 1a, middle).

As the electron relaxation time becomes even longer, the proportionality between $R_1/R_2$ and $T_{1e}$ is lost and $R_2$ relaxation dominates (Fig. 1a, right). Now, the electron relaxation time is larger than $\tau_R$ (for example, when using $Gd^{3+}$, $Mn^{2+}$, and $Cu^{2+}$ in protein NMR applications) and the effective correlation times therefore become dominated by the rotational correlation times of the nucleus–electron vector (i.e., $\tau_{c1} \approx \tau_R$ and $\tau_{c2} \approx \tau_R$). When $\omega_I\tau_R > 1$, the longitudinal and transverse paramagnetic relaxation enhancements become:

$$R_{1p} = \frac{2S(S+1)\gamma_I^2 g^2 \beta^2}{15r^6}\left(\frac{\mu_0}{4\pi}\right)^2 \times \frac{3\,\tau_r}{1+\omega_I^2\tau_r^2} \quad (10)$$

$$R_{2p} = \frac{S(S+1)\gamma_I^2 g^2 \beta^2}{15r^6}\left(\frac{\mu_0}{4\pi}\right)^2\left[4\tau_r + \frac{3\,\tau_r}{1+\omega_I^2\tau_r^2}\right] \quad (11)$$

In this situation, $R_{2p} > R_{1p}$, and the addition of such a paramagnetic agent leads to significant line broadening. We have verified that this is indeed the case by addition of gadodiamide to α-synuclein; at 2 mM the NMR spectra were significantly broadened with little effect on $R_{1p}$. Similarly, nitroxide radicals with a $T_{1e} \approx 100$ ns (Hocking et al. 2013) produce an $R_{2p}$-dominated PRE effect. The paramagnetic relaxation enhancement maintains the same overall appearance at different field strengths, although the contribution to $R_1$ is significantly reduced at higher field strengths (Fig. 1b).

## Materials and methods

### Fe(DO3A) synthesis

1,4,7-Tris(carboxymethyl)-1,4,7,10-tetraazacyclododecane (H3DO3A) was prepared according to the method described by Huskens et al. (1997). Briefly, Tri-tert-butyl 2,2′,2″-(1,4,7,10-tetraazacyclododecane-1,4,7-triyl)triacetate (0.5 g, 0.97 mmol) was dissolved in 16 mL of 20 % HCl and refluxed for 1 day. HCl was removed under reduced pressure, to yield a white solid. Absolute ethanol (8 mL) and diethylether (2 mL) were added, and the white precipitate was filtered over a glass filter, washed with an ethanol-ether (1:1) mixture (3.5 mL) and with diethylether

$(3 \times 3.5$ mL), and then dried in a stream of dry nitrogen gas to yield 0.35 g (80 %) of a white solid. The complex Fe(DO3A) was synthesized based on the procedure described by Chang et al. (1993) Briefly, $Fe(OH)_3$ (1 mmol) was prepared by reacting 1 mmol $FeCl_3$ and $H_2O$ with 3.1 mmol NaOH. $Fe(OH)_3$ was then reacted with 1 mmol of H3DO3A in water at 90 °C for 1 h under stirring. The resulting clear yellow solution was evaporated under reduced pressure to give a yellow-green solid. The compound was crystallized by dissolving the solid in 18 mL boiling ethanol containing 1 % water and cooling the solution slowly to 0 °C. The yellow crystals were collected, washed with 2.5 mL ethanol and subsequently 2.5 mL acetone. The sample was checked using elemental analysis procedure. Anal. Cald. for $C_{14}H_{23}FeN_4O_6$: C = 40.79, H = 5.98, N = 13.59. Found C = 40.56, H = 5.78, N = 13.56. The Fe(DO3A) powder was solubilized in 20 mM phosphate to stock solutions of either 100 or 300 mM and spun 15,000 g for 10 min to remove any $Fe(OH)_3$ precipitate. Insufficient buffering of the weakly acidic Fe(DO3A) material was detected by small pH-induced chemical shift changes in the NMR spectra of α-synuclein, and stocks were subsequently prepared by (1) solubilization in 250 mM ammonium bicarbonate, (2) spinning to remove $Fe(OH)_3$ precipitate, and (3) freeze-drying of the supernatant and resolubilization in 20 mM phosphate buffer. Concentrations were based on dry weight of freeze-dried powder. Small (estimated <5 %) batch-dependent amounts of uncomplexed DO3A were observed in 1D proton NMR traces.

## Protein NMR samples

### U-[$^{13}$C, $^{15}$N] α-synuclein

The chemically synthesized gene of α-synuclein was cloned into a pET25b vector, and the protein was overexpressed in *E. coli* BL21(DE3). Cells were grown in M9 minimal medium containing 1 g/L $^{13}$C-glucose and 2 g/L $^{15}$NH$_4$Cl at 37 °C with 100 μg/mL ampicillin and the expression was induced using 1 mM IPTG (isopropyl-thiogalactoside) at an OD$_{600}$ ∼ 0.6. Cells continued growing for 4 h until they reached their plateau (OD$_{600}$ ∼ 0.8–0.9).

To purify U-[$^{13}$C,$^{15}$N] α-synuclein, cell pellets were resuspended in 100 mL buffer containing 50 mM Tris–HCl (pH 8), 0.1 mM DTT, 5 mM EDTA, 1 mM PMSF (polymethanesulfonyl fluoride) and lysozyme (2 mg/g of bacterial cells). The suspension was incubated for 15 min and sonicated. After sonication, the cells were centrifuged (44,000g, 30 min and 4 °C) and streptomycin was added to the cell lysate slowly up to 5 % (w/w) at low temperature. The suspension was centrifuged (44,000×g, 30 min and 4 °C) and the supernatant was heated at 80 °C for 20 min. During the heating process, most of the proteins were

precipitated and α-synuclein, which was in the supernatant, was separated by centrifugation (44,000×g, 30 min and 4 °C). The proteins in the supernatant were precipitated using 70 % $(NH_4)_2SO_4$. The precipitated proteins were separated from the supernatant by centrifugation (44,000×g, 30 min and 4 °C). The pellet was dissolved in 20 mL buffer (50 mM Tris–HCl (pH 7.2), 1 mM PMSF, and 2 mM EDTA) and the solution was desalted using a NAP-20 column. The protein was then purified using anion exchange (Q-trap column) followed by gel filtration. The solvent of the sample was exchanged with 20 mM phosphate buffer (pH 7.4) containing 100 mM NaCl and 0.02 % azide. The purity of U-[$^{13}$C,$^{15}$N] α-synuclein was confirmed using 12.5 % SDS–PAGE.

### U-[$^{13}$C, $^{15}$N], $^2$H α-synuclein

To produce U-[$^{13}$C,$^{15}$N], $^2$H α-synuclein, *E. coli* BL21(DE3) cells were grown in M9 minimal medium containing 2 g/L $^{13}$C-D-glucose and 1 g/L $^{15}$NH$_4$Cl at 37 °C and ∼100 % $D_2O$. The expression was induced using 1 mM IPTG (isopropyl-thiogalactoside) at an OD$_{600}$ ∼ 0.6. Cells continued growing for 4 h until they reached their plateau (OD$_{600}$ ∼ 0.7–0.8). Purification of U-[$^{13}$C,$^{15}$N], $^2$H α-synuclein followed the same procedure as described above for U-[$^{13}$C,$^{15}$N] α-synuclein. The use of protonated glucose and $D_2O$ results in proteins that are ∼85 % deuterated on average, but where Cα positions are nearly 100 % deuterated as the attached atom originates directly from the medium.

### U-[$^{13}$C, $^{15}$N] C-36

The C-36 DNA sequence was cloned into the SUMO Champion$^{TM}$ vector (Life Technologies) by TA cloning of an amplified PCR fragment from the full-length $α_1$AT sequence. The in-frame fusion to the SUMO gene gives expression of SUMO-C36 from which C-36 can be liberated by treatment with the SUMO protease, resulting in a native N-terminus. The fusion protein was expressed by induction of *E. coli* BL21(DE3) cells with 1 mM IPTG, grown in M9 minimal medium containing 2 g/L $^{13}$C-glucose and 1 g/L $^{15}$NH$_4$Cl. After 4 h at 37 °C, the cells were harvested and the bacterial pellet from 1 L was incubated with 60 mL of denaturing lysis buffer (6 M GdnHCl, 20 mM phosphate buffer, 500 mM NaCl, pH 7.8) for 30 min at RT on a rotating table. The solution was then sonicated for 2 × 5 min using 0.5 s on/off pulse. After spinning at 15,000×g for 20 min, the supernatant was filtered through a 0.22 μm filter and loaded onto a pre-packed Ni–NTA column equilibrated in the same buffer. After washing 5 column volumes (CV), the buffer was changed to 8 M urea buffer (8 M urea, 20 mM phosphate, 500 mM NaCl, pH 7.8) and washed for 10 CV. A low pH wash step was

conducted in 10 CV of urea buffer equilibrated to pH 6.3 and elution of the target protein was then done with urea buffer equilibrated to pH 4.5. The low-pH fractions were pooled, trifluoroacetic acid (TFA) was added to a final concentration of 0.5 %, and the fractions were spun for 10 min at $15,000 \times g$ and then loaded onto a reverse-phase RP300 Octyl C8 HPLC column (Brownlee 250 × 10 mm), equilibrated in 0.1 % TFA with 20 % B solution (90 % Acetonitrile, 10 % 0.1 %-TFA). Elution from the column was done using a gradient of 0.4 % B/min from 35 to 60 % B. The main peak fractions containing SUMO-C-36 were pooled and lyophilized. The dry powder was solubilized in 20 mM Tris buffer (pH 8.0) containing 100 mM NaCl and 1 mM DTT. Cleavage of the fusion protein was performed o/n at RT by adding 4 U/mg target protein of the SUMO protease. During this incubation period, heavy aggregation/fibrillation took place. The sample was then added GdnHCl salt to final 6 M for complete solubilization of the aggregated protein. After acidification with 0.5 % final TFA, the sample was spun 15 min at $15,000 \times g$ and re-loaded onto the RP300 column. Elution was done by applying a gradient of 0.35 % B/min. This elution procedure resulted in separation of the C-36 peptide peak. The purity was checked by SDS-PAGE using 15 % Tricine gels and the peptide mass was validated by mass spectrometry and showed a labeling efficiency >99 %. The denaturant-assisted purification procedure was developed for C-36 to ensure minimal loss, as the peptide was very prone to aggregation. Non-cleaved SUMO-36 could be lyophilized again and subjected to a new round of cleavage. Of note, in this procedure, the SUMO protein fusion partner acts as a fast-folding solubility enhancer that makes the cleavage site accessible to the SUMO protease in the short time before aggregation takes place. Recombinant labeled C-36 (SIPPEV KFNKPFVFLMIEQNTKSPLFMGK-VVNPTQK) was solubilized from lyophilized powder in dH$_2$O, quantified and stored in stocks of 2 mg/mL at $-80$ °C. Immediately before the NMR experiments, a solution of 200 μM was prepared with a final composition of 20 mM NaH$_2$PO$_4$/Na$_2$HPO$_4$, pH 7.0, 8 % D$_2$O and 10 mM Fe(DO3A). The peptide solution was carefully transferred by use of a thin plastic pipette and all solutions were cooled to 4 °C prior to mixing to keep aggregation at a minimum. NMR experiments were run at 275 K on Bruker 500 MHz spectrometer.

## NMR experimental details

### Saturation-recovery experiments for determination of $T_1$ for water, amide and methyl protons

The $^1$H $T_1$ relaxation time of water was probed by saturation recovery with a series of delays following a pre-saturation sequence. After a given delay, only a fraction of the water magnetization was brought into the transverse

plane for detection by application of a short tapping pulse, resulting in a small tilt angle. $T_1$ values were fitted by the Topspin 3.2 relaxation module (Bruker). Amide proton envelope relaxation times were probed by 1D versions of the standard $^1$H–$^{15}$N HSQC experiment with a series of recycle delays ranging from 8 ms to 4 s. For methyl protons, a 1D version of $^1$H–$^{13}$C HSQC with a constant time period set to a minimum value (0.2 ms) was used to keep all magnetization in-phase. Amide and methyl proton envelope intensities were plotted as a function of total recovery time (recycle delay + acquisition time). The $T_1$ value was derived by parameter fitting using Kaleidagraph (fitting to the equation $M(t)/M(\infty) = A(1 - B * \exp(-t/T_1))$). $T_1$ determination was done at Fe(DO3A) concentrations of 0, 2.5, 5, 7.5, and 10 mM. The relaxivity ($s^{-1}$ mM$^{-1}$) of Fe(DO3A) was estimated by doing linear regression on the $R_1$ values plotted as a function of concentration. All these experiments were performed on the same U-[$^{15}$N,$^{13}$C] α-synuclein sample on a 500 MHz Bruker spectrometer at 275 K.

### $^1$H $T_1$ relaxation across the sequence of α-synuclein

Residue-specific amide $^1$H $T_1$ relaxation at 600 MHz (Fig. 2) was measured on an α-synuclein sample containing 0, 5 and 8 mM Fe(DO3A) using saturation recovery with a standard sensitivity-enhanced 2D $^1$H–$^{15}$N HSQC pulse sequence (Kay et al. 1992). Proton saturation was achieved using a train of 300 120° proton pulses. All spectra were recorded with 24 scans per increment and with 160 increments in the indirect domain using spectral widths of 8000 Hz ($^1$H) and 1650 Hz ($^{15}$N). The experiment was performed on a Varian Unity INOVA 600 MHz spectrometer equipped with a z-field-gradient probe at 283 K.

Residue-specific amide $^1$H $T_1$ relaxation at 500 MHz (Figs. 4, 5) was measured on an α-synuclein sample at three concentrations (0, 5 and 10 mM) of Fe(DO3A), and, for each concentration, at three temperatures (275, 283 and 293 K). Amide inversion recovery experiments were carried out as follows: Inversion of protein proton magnetization was achieved with a pulse sequence element that (1) selectively flipped the water signal to the xy-plane, (2) applying a non-selective 180° pulse, (3) returning the water magnetization to +Z, (4) waiting a variable delay time, and (5) acquisition by a standard water flip-back SE-HSQC experiment. This left the water state untouched during the inversion recovery delay. The spectra were recorded with 4 scans per increment sampling 2 K and 256 points in the direct ($^1$H) and indirect dimension ($^{15}$N), respectively, using spectral widths of 8013 Hz ($^1$H) and 1166 Hz ($^{15}$N). A total of 9 delay points were used to sample the recovery curve (from 12.5 ms to 3.2 s).
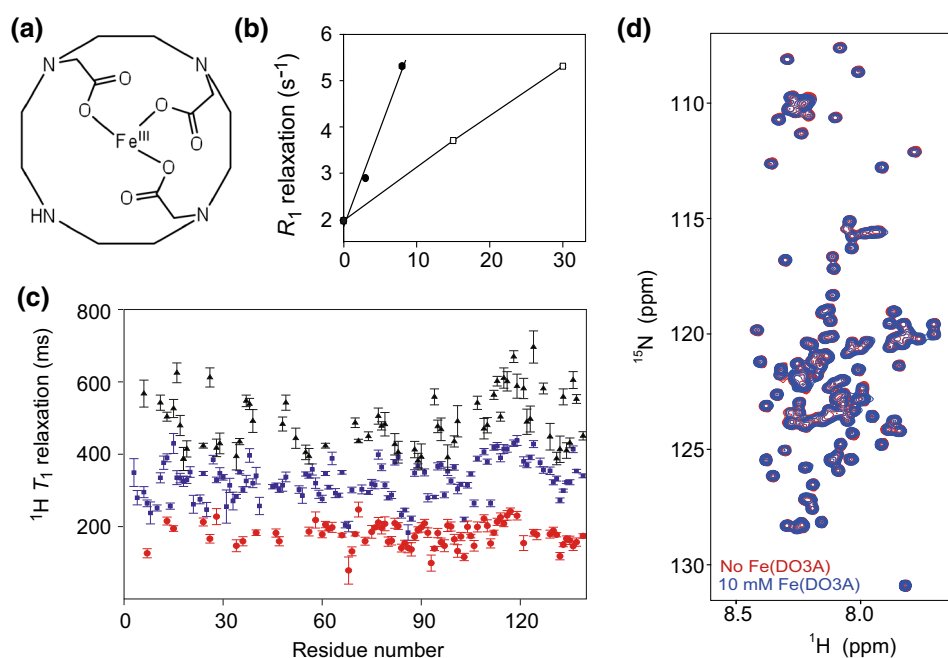
**Fig. 2** **a** Structure of the Fe(DO3A) PRE agent. **b** Average amide proton longitudinal relaxation rates ($R_1 = 1/T_1$) for α-synuclein upon the addition of Ni(DO2A) (*white squares*) and Fe(DO3A) (*filled circles*). **c** $^1$H $T_1$ of intrinsically disordered α-synuclein in the absence (*black*) and presence of 3 mM (*blue*) and 8 mM (*red*) Fe(DO3A). All experiments were performed at pH 7.4 and 10 °C at 600 MHz. **d** Overlay of $^1$H–$^{15}$N HSQC spectra for α-synuclein with (*blue*) and without (*red*) 10 mM Fe(DO3A) at 2 °C

## 2D CACO IPAP experiments

The experiments were carried out using a Bruker 950 MHz spectrometer equipped with a triple-resonance TCI cryogenic probe with a z-axis gradient coil. The spectra were acquired using 33 ($^{13}$Cα) × 512 ($^{13}$C′) complex points, with maximum evolution times of 4.5 and 54.8 ms, respectively. The carrier position was placed at 56 ppm in the $^{13}$Cα domain and 174.7 ppm in the $^{13}$C′ domain. Number of scans is 32 for each spectrum. Recycle delays of 1, 2, 3, 4, and 5 s were used for recording the 2D CACO IPAP experiments of U-[$^{13}$C,$^{15}$N], $^2$H α-synuclein. Recycle delays of 1, 1.5, 2, 2.5, 3, 4, and 5 s were used for recording these spectra in the presence of 20 mM Fe(DO3A). The lines are best fits to the saturation-recovery equation M(t)/M(∞) = 1 − exp(−t/$T_1$).

## 3D CANCO IPAP experiment

The experiments were performed using the same spectrometer as used for 2D CACO experiments. The spectra were acquired using 22 ($^{13}$Cα) × 38 ($^{15}$N) × 512 ($^{13}$C′) complex points with maximum evolution times of 3.08, 11.29, and 54.8 ms, respectively. The carrier position was placed at 56.6 ppm in the $^{13}$Cα domain, 119 ppm in the $^{15}$N domain and 174.7 ppm in the $^{13}$C′ domain. A recycle delay of 2 s and 16 scans per FID were used, giving a total experimental time of about 33 h.

## NMR spectroscopy of C-36

For rapid acquisition of both 2D and 3D experiments in an experimental setting with unknown sample half-life, we decided to continuously repeat ('loop') a set of $^1$H–$^{15}$N HSQC, $^1$H–$^{13}$C HSQC, HNCACB, and HN(CA)CO experiments, all with recycle delays of 100 ms between scans. To avoid excessive heating in the higher RF duty cycle caused by nitrogen decoupling during proton acquisition (128 ms), decoupling was changed to WALTZ16 with half the field strength, depositing 1/4th of the power (4.25 W). This was true for all but the $^1$H–$^{13}$C HSQC, where the default GARP-1 decoupling scheme had to be preserved to ensure proper carbon decoupling (4.49 W). The individual settings for the experiments were as follows, each run with 2 scans only: $^1$H–$^{15}$N HSQC: 2048 ($^1$H) × 256 ($^{15}$N) complex points, 32 ppm spectral width, carrier at 117 ppm, $^1$H aq.time 128 ms. Constant-time $^1$H–$^{13}$C HSQC: 1024 ($^1$H) × 256 ($^{13}$C) complex points, 70 ppm spectral width, carrier at 40 ppm, $^1$H aq.time 64 ms. HNCACB: 1024 ($^1$H) × 64 ($^{15}$N) × 128 ($^{13}$C) complex points, spectral widths of 26 ppm ($^{15}$N) and 75 ppm ($^{13}$C) and carriers at 119 ppm ($^{15}$N) and 42 ppm ($^{13}$C), $^1$H aq.time 73 ms. HN(CA)CO: spectral widths of 26 ppm ($^{15}$N) and 10 ppm ($^{13}$C) and carriers at 119 ppm ($^{15}$N) and 174 ppm ($^{13}$C), $^1$H aq.time 73 ms. Dummy scans were increased before the 3D experiments to a total

duration of 4–5 min to allow temperature equilibration with the short recycle delay and higher RF duty cycle. The total experimental time for one entire loop (4 experiments) was ∼3 h ($^1$H–$^{15}$N HSQC, 2 min 40 s; $^1$H–$^{13}$C HSQC, 4 min; HNCACB, 1 h 25 min; HN(CA)CO, 1 h 21 min). The series of experiments were looped 4 times and as the sample half-life was longer than expected, we also recorded hCccoNH and HcccoNH experiments and used these to validate the Cα assignment and to get the connectivity of the Hα chemical shifts. The $T_1$ value for C-36 was determined by a set of 1D $^1$H–$^{15}$N experiments with recycle delays from 8 ms to 4 s with acquisition times of 64 ms, as previously described for α-synuclein.

## Data processing and analysis

The spectra were processed using NMRPipe (Delaglio et al. 1995) and analyzed using SPARKY (Goddard and Kneller 2003) or CCPN (Vranken et al. 2005). Relaxation data were analyzed using Mathematica (Wolfram Inc) or Kaleidagraph (Synergy). Assignment of C-36 was done using NMRPipe for processing and CCPN for peak picking. All spectra were referenced according to IUPAC convention. The ncIDP software was used for prediction of C-36 random coil chemical shifts and the ncSPC software was used for calculation of secondary-structure propensity scores, available online at http://www.protein-nmr.org.

## Circular dichroism of C-36

C-36 was made by peptide synthesis and analyzed as monomer or fibril. Protein stock preparations were solubilized in $H_2O$ before use. The fibrillar material was generated by incubating 50 μM peptide in PBS at 25 °C for 5 days under mild agitation. The assessment of secondary-structure elements was done by circular dichroism spectroscopy on a Jasco J-800 spectropolarimeter using a quartz cuvette of 0.1 cm path length and a protein concentration of 25 μM. The far-UV spectra from 200 to 250 nm at 20 °C were collected 5 times, averaged and baseline corrected by subtracting a reference spectrum.

## Results and discussion

### Properties of the Fe(DO3A) chelate tested on α-synuclein

Based on the simulation of the paramagnetic contribution to the $T_1$ relaxation rate and the optimal properties of high-spin $Fe^{3+}$ for co-solute PRE, we identified the tetraazacyclododecane-1,4,7-triacetate (DO3A) as a suitable cage and produced the neutral Fe(DO3A) chelate agent (Fig. 2a). The incorporation of high-spin $Fe^{3+}$ to form a neutral complex provides the target electron relaxation times of ∼100 ps (Bertini et al. 2001) for optimal relaxivity without large $R_2$ increase. The stability of the DO3A chelate is dictated by secondary ring amine and carboxylate protonation constants (log $Ki$ = 11.59, 9.24, 4.43, and 3.48) (Kumar et al. 1994), making it applicable in the physiological pH range.

The efficacy of the agent was validated in a series of experiments with differentially labeled variants of the model IDP α-synuclein (either U-[$^{13}$C,$^{15}$N] or U-[$^{13}$C,$^{15}$N], $^2$H-labeled). The concentration-dependent relaxation contribution from Fe(DO3A) (relaxivity) was estimated by measuring $T_1$ for water, amide and methyl protons at 2 °C as a function of Fe(DO3A) concentration, yielding respective relaxivities of 0.33, 0.30, and 0.30 s$^{-1}$ mM$^{-1}$ at 500 MHz. At this temperature, amide proton exchange is minimized and the similar relaxivities found for amide and methyl protons corroborates the expected direct interaction between Fe(DO3A) and protein protons. Next, we compared the PRE effect of Fe(DO3A) on α-synuclein with that of Ni(DO2A) (Fig. 2b). The relaxivity of the two compounds at 600 MHz and 10 °C were found to be 0.43 and 0.11 s$^{-1}$ mM$^{-1}$ for Fe(DO3A) and Ni(DO2A), respectively, as measured by saturation-recovery, providing an almost fourfold increased potency of Fe(DO3A) under these circumstances. This is in accord with the expected theoretical larger PRE offered by Fe(DO3A). In addition, the result supports the preferential coordination of $Fe^{3+}$ in its high-spin state (S = 5/2) by the DO3A cage (Chang et al. 1993), as low-spin $Fe^{3+}$ is ineffective due to its short $T_{1e}$. Addition of Fe(DO3A) had no influence on NMR peak positions, indicating that no structural changes or specific binding took place upon the addition of the PRE agent, nor was any noticeable line broadening observed in the $^1$H–$^{15}$N HSQC spectrum (Fig. 2c). A quantitative analysis revealed that the addition of 10 mM Fe(DO3A) lead to a slight increase in average $^1$H linewidth, from 15.2 ± 1.4 to 16.6 ± 1.6 Hz. At the same time the change in $^{15}$N line width was insignificant, from 14.3 ± 0.5 to 14.5 ± 0.6 Hz. The Fe(DO3A) agent was evenly accessible to the entire polypeptide sequence and effectively lead to a broad reduction in the $T_1$ values (Fig. 2d).

### Amide exchange and PRE for speeding up $T_1$ relaxation

As amide proton relaxation is substantially influenced by the exchange with the solvent water at increasing temperatures (Gil et al. 2013), we next considered the contribution of this effect on both spectral quality and $R_1$ amide values of α-synuclein at 2, 10 and 20 °C (Fig. 3) and compared it to the PRE-effect obtained through Fe(DO3A) (Fig. 4). For IDRs, the temperature-mediated decrease of apparent $T_1$ values through solvent exchange offers a possible strategy for

lowering the interscan delay by keeping water along $+Z$ during acquisition, resulting in immediate relaxation of the amide protons upon exchange. Unfortunately, as seen in Fig. 3, rapid exchange may concomitantly lead to sensitivity and signal loss. The quantitative assessment of the temperature effect on the transverse relaxation rates was performed through a series of pseudo 3D inversion recovery experiments. For fast-exchanging residues like glycines (exemplified by Group A: G31, G41, G68, G73, G86 and T92) the average $R_1$ went from 10.8 s$^{-1}$ at 2 °C to 24.1 s$^{-1}$ at

10 °C with too poor spectral quality for determination at 20 °C (Fig. 3a, c). For other residue types (Group B: L38, V71, E83, A89, K96, A107, D119), the average $R_1$ went from 3.5 s$^{-1}$ at 2 °C to 14.2 s$^{-1}$ at 20 °C, still offering fair spectral quality. As intrinsic solvent exchange rates in IDPs typically vary by two orders of magnitude due to sequence-dependent amide p$K_a$ differences, this approach elicits a heterogeneous response, which may make it challenging to balance positive and negative relaxation effects in practice. For comparison, we extracted $R_1$ rates of the amide groups in
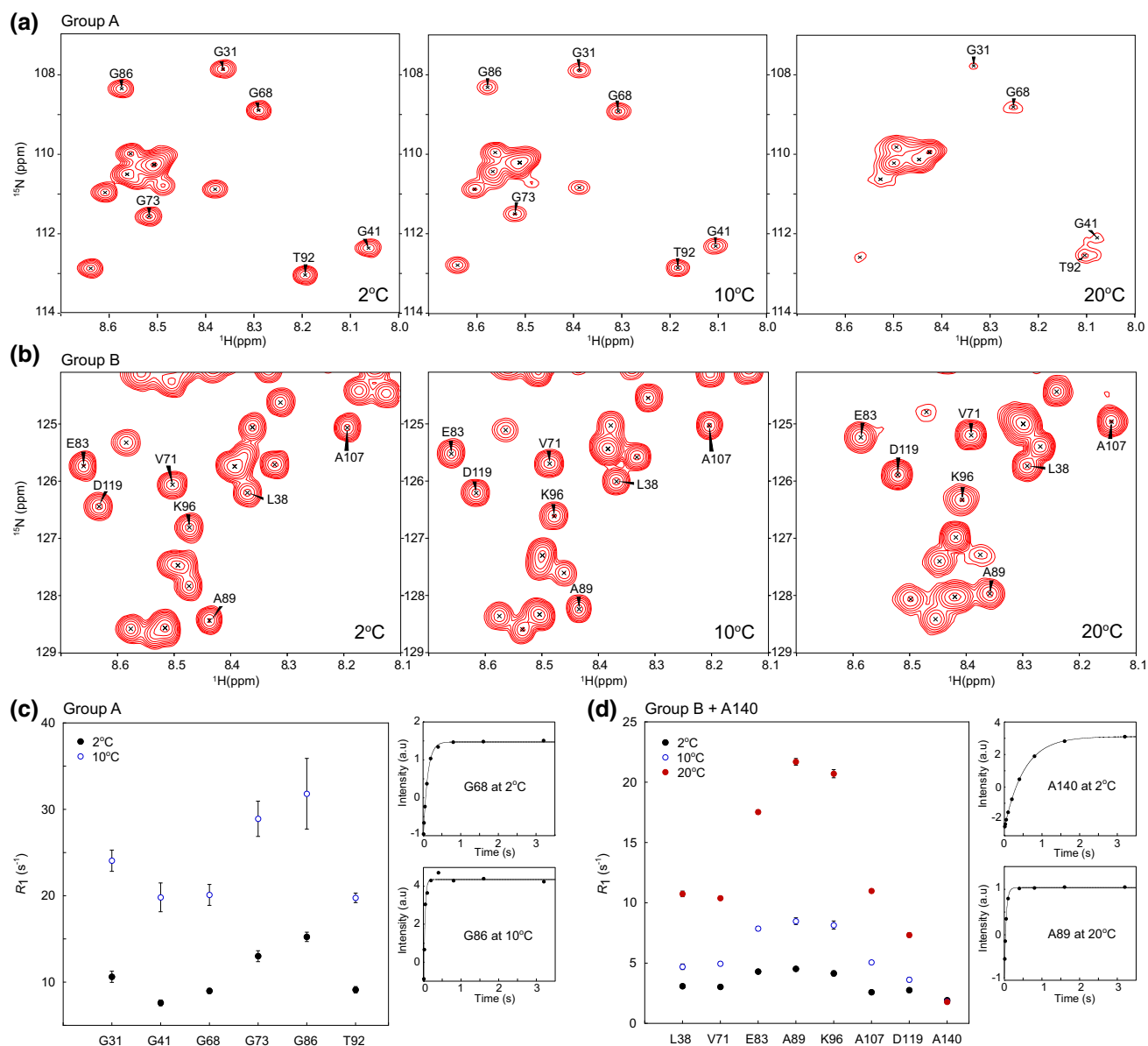


**Fig. 3** **a** Spectral changes observed in the glycine-rich region of α-synuclein with increasing temperature (group A). The fast exchange of these amide groups severely impacts sensitivity at 20 °C. **b** Spectral changes observed in mixed region with increasing temperature (group B). **c** $R_1$ values of group A amide groups at 2 and 10 °C with the fit error indicated by *black bars*. Inversion recovery plots of G68 at 2 °C (lowest fit error) and G86 at 20 °C (largest fit error) are shown to the *right*. **d** $R_1$ values of group B, incl. A140 at 2, 10 and 20 °C with fit error indicated by *black bars*. Inversion recovery plots of A140 at 2 °C (lowest $R_1$ value) and A89 at 20 °C (largest $R_1$ value) are shown to the *right*. All experiments were carried out on α-synuclein at pH 7.4 at 500 MHz
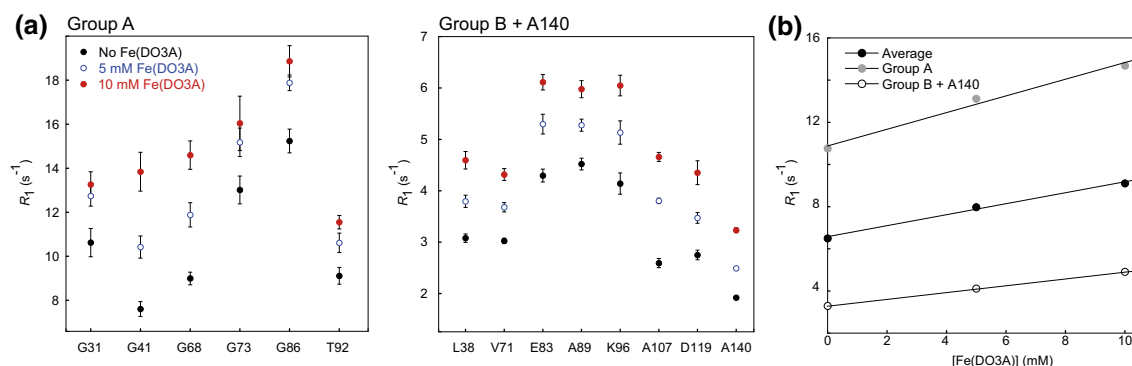
**Fig. 4** **a** $R_1$ rates in group A (*left*) and group B (*right*) measured by inversion recovery at 2 °C with addition of Fe(DO3A) to indicated final concentrations. Fit errors are shown as *black bars*. **b** Average rates plotted as a function of Fe(DO3A) concentration giving linear coefficients (relaxivities) of 0.39, 0.16 and 0.26 $s^{-1}$ $mM^{-1}$ for group A and group B, incl. A140, and the average, respectively

region A and B in the presence of 5 and 10 mM Fe(DO3A) at 2 °C (Fig. 4a), where the amide exchange rate is minimized. For all residues, a clear PRE effect was observed, including A140, which is not able to undergo exchange-mediated relaxation. The relaxivities for residues in group A and B vary (Fig. 4b). Although not further investigated here, the origin of these variations should likely be sought in sequence-dependent differences in the distance of closest approach of the paramagnetic agent. The average relaxivity of 0.26 $s^{-1}$ $mM^{-1}$ matches well with the previously stated amide envelope relaxivity of 0.30 $s^{-1}$ $mM^{-1}$ at 2 °C and 500 MHz.

## Application of Fe(DO3A) in proton-less NMR spectroscopy

As Fe(DO3A) is a potent PRE agent, it can increase the relaxation of nuclei with lower magnetogyric ratio, like $^{13}$C, at reasonable agent concentrations. Indeed, we are able to demonstrate accelerated, sensitivity-improved proton-less 2D and 3D $^{13}$C NMR spectroscopy for perdeuterated α-synuclein. Upon the addition of 20 mM Fe(DO3A), the average magnetization recovery time of the deuterated $^{13}$Cα nuclei is reduced from 2.5 to 1.1 s (Fig. 5a). This implies that the recycle delay can be reduced to obtain a signal gain of up to a factor 2.2 at this concentration (Fig. 5b), resulting in sensitivity-enhanced $^{13}$C-detected spectra (Fig. 5c). Equivalently, the sensitivity gain could be exchanged for a fivefold reduction in total experiment time. The addition of 20 mM Fe(DO3A) did not lead to measurable line broadening, as verified by 2D CACO and 3D CANCO NMR spectroscopy (Fig. 5c, d).

## Application of Fe(DO3A) to study a highly fibrillogenic peptide

Having established Fe(DO3A) as a powerful PRE agent for IDPs, we turned to the application of this agent to gain insight into the early amyloid conversion process of the highly amyloidogenic C-36 peptide of human α$_1$-antitrypsin (α$_1$AT). This proteolytically generated C-terminal peptide of 36 amino acid residues is found in several bodily fluids in vivo and readily fibrillates at physiological pH in vitro (Dichtl et al. 2000; Janciauskiene et al. 1995; Johansson et al. 1992). The C-36 peptide fragment forms part of a buried β-sheet arrangement in the context of full-length α$_1$AT (Elliott et al. 2000) (Fig. 6a) and had not previously been structurally characterized in isolation. Therefore, we speculated that this bioactive peptide might form β-strand motifs in solution that could predispose it to amyloid fibril formation. Circular dichroism suggested a large component of random coil and potentially some minor β-sheet structure, completely converting to a β-sheet arrangement upon fibrillation (Fig. 6b) and further details of both its solution structural propensity and is amyloidogenic property could be revealed by liquid-state NMR spectroscopy. Unfortunately, in our first attempts to study C-36 by NMR, aggregation occurred within the first few hours after application of the sample to the NMR tube. Fast aggregation and the absence of a sufficiently long-lived (pseudo)-equilibrium state, as observed in several other systems (Fawzi et al. 2010; Peterson et al. 2008; Svane et al. 2008; Wang et al. 2011), therefore prompted the use of co-solute PRE for enabling rapid acquisition of the necessary experimental data within the sample half-life without compromising sensitivity.

Recombinant C-36 peptide was freshly prepared at 200 μM in cold (4 °C) phosphate buffer, pH 7.0, containing 10 mM Fe(DO3A) and then carefully applied to the bottom of the NMR tube. The presence of the Fe(DO3A) agent reduced the amide proton $T_1$ relaxation time to 150 ms (Fig. 7b), allowing a reduction of the recycle delay to 100 ms, giving a total recovery time (recycle delay + acquisition) of 164 ms, close to the optimal value $1.3 \times T_1$ (Ernst et al. 1987). A well-resolved $^1$H–$^{15}$N HSQC spectrum could be recorded in 2.5 min, and within 3 h, data sets of
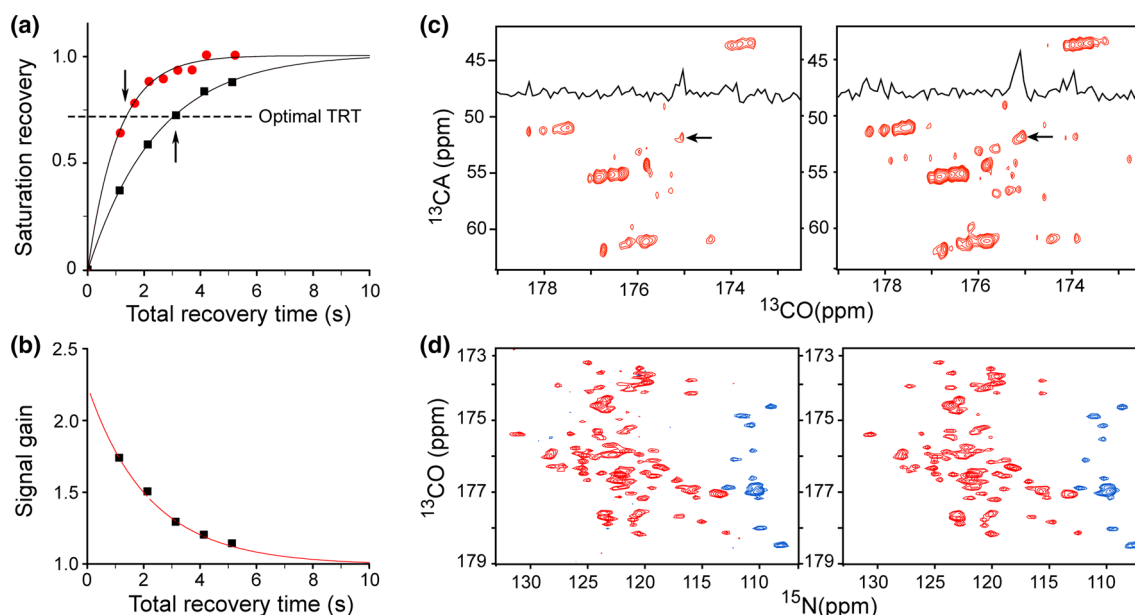
**Fig. 5** **a** Saturation recovery plot of the signal intensity in 2D CACO spectra of U-[$^{13}$C,$^{15}$N], $^2$H-labeled $\alpha$-synuclein with (*red circles*) and without (*black squares*) 20 mM Fe(DO3A) as a function of total recovery time (TRT = aquisition time + recycle delay). Maximum signal-to-noise per unit time is obtained when (TRT/$T_1$)$_{opt}$ = 1.269, where M(t)/M($\infty$) = 0.72 (*dashed line*). The optimal total recovery times equal 1.4 and 3.2 s for the situations with and without Fe(DO3A), respectively, as indicated by *black arrows*. **b** Relative sensitivity gain for 2D CACO spectroscopy of $\alpha$-synuclein upon addition of 20 mM Fe(DO3A) as a function of the total recovery time. The number of transients has been adjusted to achieve the same total experimental time. **c** 2D CACO spectra of U-[$^{13}$C,$^{15}$N],$^2$H $\alpha$-synuclein in the absence (*left*) and in the presence (*right*) of 20 mM Fe(DO3A) recorded with a recycle delay of 1 s. The spectrum is shown to the same absolute intensity to visualize the gain in sensitivity. **d** 2D NCO projection of 3D CANCO spectra recorded with a recycle delay of 2 s in the absence (*left*) and presence (*right*) of 20 mM Fe(DO3A). The spectra were scaled to the same nominal sensitivity to show that Fe(DO3A) does not cause chemical shift changes. Only a small peak shift is seen for His50, which is caused by a slight drop in pH from 7.3 to 6.9 due to the large amount of Fe(DO3A) and insufficient buffer capacity
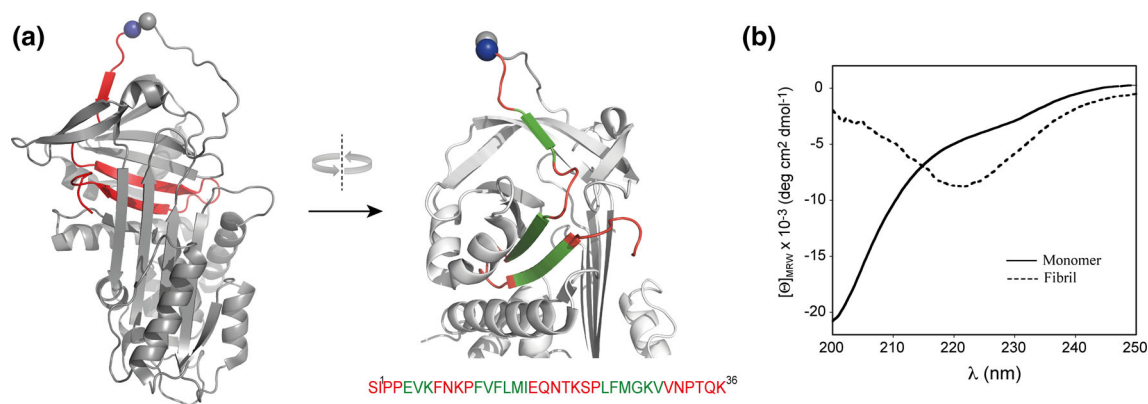


**Fig. 6** **a** Location of the C-36 peptide (*red*) in the context of native $\alpha_1$-antitrypsin (PDB ID: 1QLP) (*left*). The cleavage site for target proteases is indicated by *spheres* and marks the beginning of C-36 (*blue sphere*). The C-36 peptide forms three $\beta$-strands in the context of full-length $\alpha_1$-antitrypsin with sequences EVK, FVFLMI and LFMGKV, respectively (shown in *green*) (*right*). **b** Analysis of conformational states of C-36 in phosphate buffer by circular dichroism (CD) spectroscopy. CD signals are plotted as mean residue ellipticity ([Q]$_{MRW}$) against wavelength. The *solid line* is the spectrum of monomeric peptide, which is largely disordered. The *dotted line* is the spectrum of C-36 fibrils, which display a clear $\beta$-sheet signal from 215 to 230 nm

sufficient sensitivity were acquired for complete backbone assignment, including 2D $^1$H–$^{15}$N HSQC and $^1$H–$^{13}$C HSQC and 3D HN(CA)CO and HNCACB. The fully assigned $^1$H–$^{15}$N HSQC spectrum is shown in Fig. 7a.

The 1D amide envelope trace from $^1$H–$^{15}$N HSQC spectra recorded at various time points was used to probe the disappearance of C-36 monomer from the solution (Fig. 7c). Monomer loss displayed a sigmoidal relationship, as

typically seen in fibrillating systems. Apparently, careful sample handling and low temperature extended the useful window with only modest signal decay to 20 h for the current sample. Small variations in surface contact, liquid flow and vibrations during sample application may all have had significant impact on the nucleation rate constants and thereby limited sample stability to <4 h for our initial NMR samples.

The relatively small dispersion of the amide proton shifts, as shown in the $^1$H–$^{15}$N HSQC spectrum (Fig. 7a), immediately suggested a large degree of disorder, and lack of a persistent overall fold. This was corroborated by the low RMSD between the experimental chemical shifts and the neighbor-corrected random coil values for Cα and Cβ (Fig. 7d). The secondary chemical shifts of all assigned resonances (H$_N$, Hα, N, Cα, Cβ and CO) were weighted with their predictive power towards β-sheet or α-helix structure, resulting in a compiled secondary-structure propensity plot (Fig. 7e). This conclusively demonstrated that only very weak deviations from random coil structure are present in the monomeric C-36, indicating that it should be regarded as an intrinsically disordered peptide. Of note, the observed weak propensities are primarily of β-sheet character and located in two regions towards either end of the peptide. For the N-terminal region, this aligns relatively well with the sequence elements involved in β-sheet

formation in the native structure of full-length α$_1$-antitrypsin, as shown below the plot. The peptide fragment FVFLM has been shown to form amyloid fibrils on its own (Janciauskiene et al. 1995) and due to its high hydrophobic content, this region could fuel or initiate the primary β-sheet aggregation of the entire C-36 as well. The presence of four positively charged lysine and five proline residues likely increases the energetic barriers for the initial β-sheet formation for α1-AT in the free form. How the various sequence stretches are arranged in the mature fibrillar form will be the aim of future studies. The analysis of the highly fibrillogenic C-36 peptide by liquid-state NMR allowed residue-specific monitoring of changes during the course of fibrillation as a probe for aggregation-prone intermediate populations or fibril exchange effects. Overlays of $^1$H–$^{15}$N and $^1$H–$^{13}$C HSQC spectra recorded at various time points did, however, not show any changes in peak positions or line widths. Also, the decay in cross peak intensities was homogenous along the sequence (data not shown). This has two possible explanations: (1) The fraction of aggregation-prone monomeric or low oligomeric species with altered chemical shifts or correlation times is too low to be observed in the background of the residual monomeric population, or (2) Conversion from monomer to a pre-fibrillar state or addition to existing fibrils is a rapid and direct process involving no kinetically stable intermediate
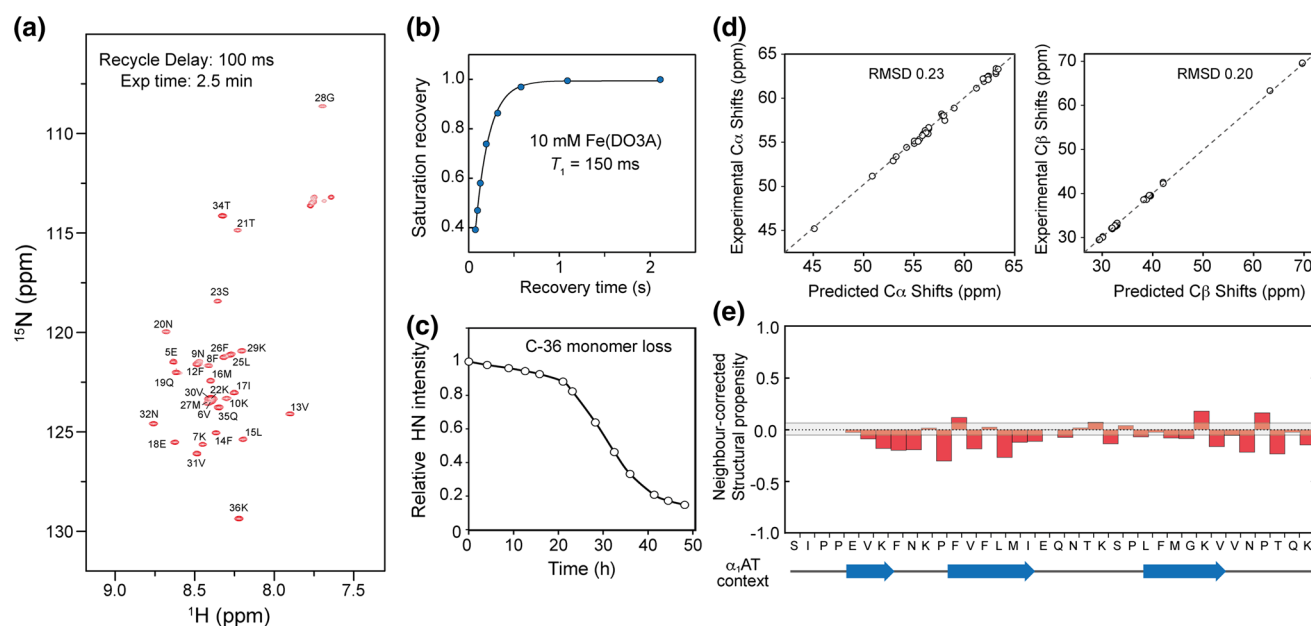


**Fig. 7** **a** $^1$H–$^{15}$N HSQC spectrum of C-36 recorded in 2.5 min with indicated residue assignments. **b** The $T_1$ relaxation time was determined by comparing relative amide envelope intensities as a function of total recovery time. **c** The fibrillation of C-36 in the NMR tube was probed by monomer loss using the $^1$H–$^{15}$N envelope intensities at different time points. **d** Neighbor-corrected random-coil chemical shifts for C-36 were predicted from the ncIDP database

(Tamiola et al. 2010) and plotted against experimental values for Cα and Cβ. **e** The secondary-structure propensity for C-36 was calculated with the ncSPC software (Tamiola and Mulder 2012) and displayed for each residue position. No apparent high-scoring elements are present, only weak β-sheet propensities are observed. The C-36 secondary structure in the context of full-length α$_1$AT is illustrated below the plot

structures visible by NMR spectroscopy in the current experimental design. In any case, the hydrophobic stretches and the weak β-sheet propensity of the peptide could explain its predisposition to amyloid formation, whether going through intermediate aggregate assemblies or directly to the more energetically favored fibrillar form.

## Conclusion

In this study, we have shown that Fe(DO3A) is an optimal paramagnetic agent for biomolecular NMR spectroscopy. It is effective at low concentrations, not liable to bind specifically to polypeptides and significantly reduces the protein $^1H$ and $^{13}C$ $T_1$ spin relaxation times without concomitant line broadening. The use of high-spin $Fe^{3+}$ to form the Fe(DO3A) agent was based on a solid rationale, and the agent has significantly better relaxation characteristics than PRE agents used for $T_1$ relaxation enhancement to date. The PRE effect is fully tuneable by the concentration of Fe(DO3A) and could be combined with SOFAST and BEST pulse sequences. In addition, the agent is sufficiently potent to reduce the necessary interscan delay for proton-less NMR experiments, and can be applied to perdeuterated samples, where long relaxation times are typically encountered. Employment of Fe(DO3A) to study a highly fibrillogenic peptide demonstrates the advantageous use of this PRE-agent for unstable aggregating systems. By reduction of the necessary recycle delay, a suite of multidimensional experiments could be performed within the lag-time of the fibrillation reaction. The full assignment of C-36 in solution provides the first insight into the secondary-structure propensities that might direct its fibrillation and which could possibly also be important for its bioactivity. The ability of Fe(DO3A) to effectively increase proton or carbon longitudinal relaxation rates can thus aid in obtaining all the necessary spectra for assignment purposes for systems limited by their short half-lives or available experimental time. Additionally, Fe(DO3A) can be used for profiling chemical shift changes with enhanced time resolution or be employed in more elaborate experiments to characterize the existence and properties of transient and sparsely populated conformational states in aggregation, oligomerization and fibrillation (Sekhar and Kay 2013). Fe(DO3A) is generally applicable to accelerate and boost the sensitivity of NMR spectroscopy and should find its use in the contemporary structural analysis of IDPs and aggregating systems and in the probing of solvent exposure in folded proteins.

## References

Abragam A (1961) The principles of nuclear magnetism. International series of monographs on physics. Clarendon Press, Oxford

Bermel W, Bertini I, Felli I, Piccioli M, Pierattelli R (2006a) 13C-detected protonless NMR spectroscopy of proteins in solution. Prog Nucl Magn Reson Spectrosc 48:25–45

Bermel W, Bertini I, Felli IC, Lee YM, Luchinat C, Pierattelli R (2006b) Protonless NMR experiments for sequence-specific assignment of backbone nuclei in unfolded proteins. J Am Chem Soc 128:3918–3919

Bertini I, Luchinat C, Parigi G (2001) Solution NMR of paramagnetic molecules: applications to metallobiomolecules and models, vol 2. Elsevier, Amsterdam

Cai S, Seu C, Kovacs Z, Sherry AD, Chen Y (2006) Sensitivity enhancement of multidimensional NMR experiments by paramagnetic relaxation effects. J Am Chem Soc 128:13474–13478

Caravan P (2009) Protein-targeted gadolinium-based magnetic resonance imaging (MRI) contrast agents: design and mechanism of action. Acc Chem Res 42:851–862

Chang CA, Francesconi LC, Malley MF, Kumar K, Gougoutas JZ, Tweedle MF (1993) Synthesis, characterization, and crystal structure of M(DO3A) (M = Fe, Gd) and Na[M(DOTA)] (M = Fe, Y, Gd). Inorg Chem 32:3501–3508

Delaglio F, Grzesiek S, Vuister GW, Zhu G, Pfeifer J, Bax A (1995) NMRPipe: a multidimensional spectral processing system based on UNIX pipes. J Biomol NMR 6:277–293

Dichtl W, Moraga F, Ares MP, Crisby M, Nilsson J, Lindgren S, Janciauskiene S (2000) The carboxyl-terminal fragment of alpha1-antitrypsin is present in atherosclerotic plaques and regulates inflammatory transcription factors in primary human monocytes. Mol Cell Biol Res Commun 4:50–61. doi:10.1006/mcbr.2000.0256

Diercks T, Daniels M, Kaptein R (2005) Extended flip-back schemes for sensitivity enhancement in multidimensional HSQC-type out-and-back experiments. J Biomol NMR 33:243–259

Elliott PR, Pei XY, Dafforn TR, Lomas DA (2000) Topography of a 2.0 Å structure of alpha1-antitrypsin reveals targets for rational drug design to prevent conformational disease. Protein Sci 9:1274–1281. doi:10.1110/ps.9.7.1274

Ernst RR, Bodenhausen G, Wokaun A (1987) Principles of nuclear magnetic resonance in one and two dimensions. International series of monographs on chemistry, vol 14. Clarendon Press, Oxford

Fawzi NL, Ying J, Torchia DA, Clore GM (2010) Kinetics of amyloid beta monomer-to-oligomer exchange by NMR relaxation. J Am Chem Soc 132:9948–9951. doi:10.1021/ja1048253

Freed JH (1978) Dynamic effects of pair correlation-functions on spin relaxation by translational diffusion in liquids. 2. Finite jumps and independent T1 processes. J Chem Phys 68:4034–4037. doi:10.1063/1.436302

Gil S, Hosek T, Solyom Z, Kummerle R, Brutscher B, Pierattelli R, Felli IC (2013) NMR spectroscopic studies of intrinsically disordered proteins at near-physiological conditions. Angew Chem Int Ed Engl 52:11808–11812. doi:10.1002/anie.201304272

Goddard TD, Kneller DG (2003) SPARKY 3. University California, San Fransisco

Hocking HG, Zangger K, Madl T (2013) Studying the structure and dynamics of biomolecules by using soluble paramagnetic probes. ChemPhysChem 14:3082–3094. doi:10.1002/cphc.201300219

Hsu ST, Bertoncini CW, Dobson CM (2009) Use of protonless NMR spectroscopy to alleviate the loss of information resulting from exchange-broadening. J Am Chem Soc 131:7222–7223

Huskens J, Torres DA, Kovacs Z, Andre JP, Geraldes CF, Sherry AD (1997) Alkaline earth metal and lanthanide(III) complexes of ligands based upon 1,4,7,10-tetraazacyclododecane-1,7-bis(acetic acid). Inorg Chem 36:1495–1503

Janciauskiene S, Carlemalm E, Eriksson S (1995) In vitro fibril formation from alpha 1-antitrypsin-derived C-terminal peptides. Biol Chem Hoppe-Seyler 376:415–423

Johansson J, Grondal S, Sjovall J, Jornvall H, Curstedt T (1992) Identification of hydrophobic fragments of alpha 1-antitrypsin and C1 protease inhibitor in human bile, plasma and spleen. FEBS Lett 299:146–148

Kay LE, Keifer P, Saarinen T (1992) Pure absorption gradient enhanced heteronuclear single quantum spectroscopy with improved sensitivity. J Am Chem Soc 114:10633–10635

Kumar K, Chang CA, Francesconi LC, Dischino DD, Malley MF, Gougoutas JZ, Tweedle MF (1994) Synthesis, stability, and structure of gadolinium(Iii) and yttrium(Iii) macrocyclic poly(-amino carboxylates). Inorg Chem 33:3567–3575. doi:10.1021/Ic00094a021

Kupce E, Freeman R (2004) Fast reconstruction of four-dimensional NMR spectra from plane projections. J Biomol NMR 28:391–395

Marion D (2005) Fast acquisition of NMR spectra using Fourier transform of non-equispaced data. J Biomol NMR 32:141–150

Pervushin K, Vogeli B, Eletsky A (2002) Longitudinal (1)H relaxation optimization in TROSY NMR spectroscopy. J Am Chem Soc 124:12898–12902

Peters JA, Huskens J, Raber DJ (1996) Lanthanide induced shifts and relaxation rate enhancements. Prog Nucl Magn Reson Spectrosc 28:221–350

Peterson DW, Zhou H, Dahlquist FW, Lew J (2008) A soluble oligomer of tau associated with fiber formation analyzed by NMR. Biochemistry 47:7393–7404. doi:10.1021/bi702466a

Pintacuda G, Otting G (2002) Identification of protein surfaces by NMR measurements with a paramagnetic Gd(III) chelate. J Am Chem Soc 124:372–373

Sakhaii P, Haase B, Bermel W, Kerssebaum R, Wagner GE, Zangger K (2013) Broadband homodecoupled NMR spectroscopy with enhanced sensitivity. J Magn Reson 233:92–95. doi:10.1016/j.jmr.2013.05.008

Schanda P, Van Melckebeke H, Brutscher B (2006) Speeding up three-dimensional protein NMR experiments to a few minutes. J Am Chem Soc 128:9042–9043

Schmit JD, Ghosh K, Dill K (2011) What drives amyloid molecules to assemble into oligomers and fibrils? Biophys J 100:450–458. doi:10.1016/j.bpj.2010.11.041

Sekhar A, Kay LE (2013) NMR paves the way for atomic level descriptions of sparsely populated, transiently formed biomolecular conformers. Proc Natl Acad Sci USA 110:12867–12874. doi:10.1073/pnas.1305688110

Svane AS, Jahn K, Deva T, Malmendal A, Otzen DE, Dittmer J, Nielsen NC (2008) Early stages of amyloid fibril formation studied by liquid-state NMR: the peptide hormone glucagon. Biophys J 95:366–377. doi:10.1529/biophysj.107.122895

Takeuchi K, Heffron G, Sun ZY, Frueh DP, Wagner G (2010) Nitrogen-detected CAN and CON experiments as alternative experiments for main chain NMR resonance assignments. J Biomol NMR 47:271–282

Tamiola K, Mulder FAA (2012) Using NMR chemical shifts to calculate the propensity for structural order and disorder in proteins. Biochem Soc Trans 40:1014–1020. doi:10.1042/BST20120171

Tamiola K, Acar B, Mulder FAA (2010) Sequence-specific random coil chemical shifts of intrinsically disordered proteins. J Am Chem Soc 132:18000–18003

Theillet FX, Binolfi A, Liokatis S, Verzini S, Selenko P (2011) Paramagnetic relaxation enhancement to improve sensitivity of fast NMR methods: application to intrinsically disordered proteins. J Biomol NMR 51:487–495

Uversky V, Longhi S (2010) Instrumental analysis of intrinsically disordered proteins. Wiley, New York

Vranken WF et al (2005) The CCPN data model for NMR spectroscopy: development of a software pipeline. Proteins 59:687–696. doi:10.1002/prot.20449

Wang W et al (2011) A soluble alpha-synuclein construct forms a dynamic tetramer. Proc Natl Acad Sci USA 108:17797–17802. doi:10.1073/pnas.1113260108